Received: 23 June 2021 | Revised: 25 October 2021 | Accepted: 16 November 2021

DOI: 10.1002/aic.17549

THERMODYNAMICS AND MOLECULAR-SCALE PHENOMENA

AIChE JOURNAL

Enhancing electrocatalytic N_2 reduction via tailoring the electric double layers

Haolan Tao[1] | Cheng Lian[1,2] | Hao Jiang[3] | Chunzhong Li[1,3] | Honglai Liu[1] | René van Roij[2]

[1]State Key Laboratory of Chemical Engineering, Frontiers Science Center for Materiobiology and Dynamic Chemistry, Shanghai Engineering Research Center of Hierarchical Nanomaterials, and School of Chemical Engineering, East China University of Science and Technology, Shanghai, China

[2]Institute for Theoretical Physics, Center for Extreme Matter and Emergent Phenomena, Utrecht University, Utrecht, The Netherlands

[3]Key Laboratory for Ultrafine Materials of Ministry of Education, School of Materials Science and Engineering, East China University of Science and Technology, Shanghai, China

Correspondence
Cheng Lian and Honglai Liu, State Key Laboratory of Chemical Engineering, Frontiers Science Center for Materiobiology and Dynamic Chemistry, Shanghai Engineering Research Center of Hierarchical Nanomaterials, and School of Chemical Engineering, East China University of Science and Technology, Shanghai 200237, China.
Email: liancheng@ecust.edu.cn (C.L.) and hlliu@ecust.edu.cn (H.L.)

Hao Jiang, Key Laboratory for Ultrafine Materials of Ministry of Education, School of Materials Science and Engineering, East China University of Science and Technology, Shanghai 200237, China.
Email: jianghao@ecust.edu.cn

Funding information
EU-FET project NANOPHLOW, Grant/Award Number: REP-766972-1; National Natural Science Foundation of China, Grant/Award Numbers: 91834301, 22078088, 51621002; Netherlands Organization for Scientific Research (NWO); Shanghai Rising-Star Program, Grant/Award Number: 21QA1401900

Abstract

The electrocatalytic nitrogen reduction reaction (NRR) for NH_3 synthesis is still far from being practical and competitive with the common Haber–Bosch process. The rational design of highly selective NRR electrocatalyst is therefore urgently needed, which requires a deep understanding of both the electrode–electrolyte interface and the mass transport of reactants. Here, we develop a theoretical framework that includes electric double layer (EDL), mass transport, and the NRR kinetics. This allows us to evaluate the roles of near-electrode environment and N_2 diffusion on the NRR selectivity and activity. The EDL, as the immediate reaction environment, remarkably impedes the diffusion of N_2 to the cathode surface at high electrode potentials, which explains experimental observations. This article also gives microscopic insights into the interplay between N_2 diffusion and reaction activity under the nano-confinement, providing theoretical guidance for future design of advanced NRR electrocatalytic systems.

KEYWORDS
electric double layer, electrocatalytic N_2 reduction, modified Poisson-Nernst-Planck equations, reaction-transport process

1 | INTRODUCTION

Due to the rapid growth of the world's population, the concomitant increase of the energy consumption as well as the disastrous impediments caused by climate change, the development of sustainable and fossil-free pathways for the production of fuels and chemicals is particularly vital to effectively reduce the global CO_2 emission.[1] Ammonia (NH_3) is not only an important chemical to produce fertilizers, dyes, explosives, and resins,[2–4] but it is also an ideal energy carrier and storage intermediate for renewable energy sources.[5] However, industrial-scale Haber–Bosch synthesis of ammonia ($N_2 + 3H_2 \rightarrow 2NH_3$) requires such high temperatures (400–500°C) and pressures (10–30 MPa) that this process is responsible for more than 1% of the global energy consumption and utilization of half of the global hydrogen production with serious greenhouse gas emission.[6,7]

In the search for alternatives, electrocatalytic reduction of nitrogen has shown promising potential as an environmentally benign and highly sustainable alternative for NH_3 synthesis at ambient conditions.[8–10]

Haolan Tao and Cheng Lian contributed equally to this study.

Despite significant efforts to improve the nitrogen reduction reaction (NRR) $N_2 + 6e^- + 6H^+ \rightarrow 2NH_3$ in an electrochemical fashion, for instance by designing novel nanostructured electrodes, cell configurations, catalysts and electrolytes to enhance the faradaic efficiency, the reported performances are still far away from those of the Haber–Bosch process.[11,12] One challenge for the improvement of the electrochemical NRR is the strong competition of the hydrogen evolution reaction (HER) $2H^+ + 2e^- \rightarrow H_2$ that reduces the proton into H_2 at the cathode.[13–17] To address this issue, one primary strategy is the design of the electrocatalyst itself to suppress HER while supporting an optimized NRR to ammonia.[18] Currently, noble metal-containing electrocatalysts (Au,[19,20] Ru,[21,22] etc.) as well as nonnoble metal-based electrocatalysts (Bi,[23] Ti,[24] etc.) are emerging more widely. They are designed with well-known strategies, such as morphological control of size or shape, bimetallic composition, and heteroatom doping, and they are generally supported by carbon-based materials. Due to the low coordination environment and the high atom-utilization, single atom catalysts (SACs) show great potential for the suppression of the undesirable HER,[25] which are prepared by bonding the transition metal atoms (Fe, Ru, Mo, etc.) to the appropriate supports with N-coordination or O-coordination.[26,27] Recently, the Cu SACs also exhibit an outstanding performance with high NH_3 yield rate and faradaic efficiency, arising from the $Cu - N_2$ sites and the rich active sites anchored in porous N-doped carbon.[28] The introduction of Cu into single-atom Pd sites can form diatomic Pd-Cu sites, leading to activated protonation of N_2 and suppressed hydrogen evolution.[29] Also, a Mott–Schottky interface contact has been designed between the electron-deficient Cu nanoparticles and a semi-conductive polyimide support, which retards the HER process in basic electrolytes.[30] Furthermore, another promising strategy that can mitigate the competing H_2 evolution is to limit the proton accessibility,[31] which can be achieved by modulating the electrolyte pH, adding alkali metal cations into electrolytes, and building a hydrophobic protection layer on the surface of electrocatalysts.[23,32] More recently, the proton-filtering covalent organic frameworks on the catalyst surface are designed to obtain a suppressed proton supply and a greatly enhanced nitrogen flux, and thus realizing a high Faradaic efficiency in an acidic aqueous solution under ambient conditions.[33] The adoption of a nonaqueous electrolyte, which avoids the large availability of protons, is also expected to overcome the obstacle.[34] Meanwhile, the lithium-mediated strategy can be implemented to reach high Faradaic efficiency, which requires a further improvement of stability and energy efficiency.[35] Moreover, the quite low solubility of N_2 in aqueous electrolytes limits the reactive and diffusive adsorption on the catalyst surface,[36] which further challenges the possibility of a high NRR performance. Recent progress, however, includes the development of a gas diffusion electrode based on a stainless steel cloth to overcome gas transport limitations for high-current ammonia electrosynthesis in nonaqueous solvents.[34] In addition, due to the extremely low yield of ammonia as observed in many experiments,[37] the ammonia contamination in the experimental environment and materials cannot be ignored. Therefore, rigorous control protocols and confirmatory experimental methods are required to reliably detect and quantify the ammonia from nitrogen reduction.[37–39]

The combination of theoretical guidance and experimental studies has proven to be an effective strategy to partially overcome the above obstacles.[1] According to calculations within electronic Density Functional Theory (DFT), active elemental metal catalysts perform optimally when they bind reaction intermediates such as $*N_2H$ and $*NH_2$ (where the asterisk * denotes an adsorption site on the catalyst surface) neither too strongly nor too weakly.[17,40] The high-performance transition metal SACs, which require a suitable matching of the support and the metal center, can be screened by evaluating their intrinsic activity through extensive DFT computations.[41] More recently, a combination of a constant electrode potential model and microkinetic modeling is used to investigate the potential-dependent competition between NRR and HER, providing a theoretical understanding on the challenge of low selectivity at high potentials.[42] However, to keep pace with the experimental strategies, theoretical studies should not only focus on screening and improving the potential catalysts for their electrochemical properties, but also pay attention to optimize the reaction environment and the (thermo-)dynamic conditions, involving the nature of the electrolyte, the structure of the electrolyte–electrode interface, and, very importantly, the mass transport of the reactants.[1,11] For instance, recent research demonstrated that the addition of potassium ions in electrolyte not only stabilizes key nitrogen-reduction intermediates to enhance NRR, but also significantly suppresses HER by slowing down proton transport from the bulk solution to the electrode surface.[23] The electric double layer (EDL), as the local reaction environment, plays a significant role in determining the NRR activity and selectivity,[43] which can be optimized by varying electrolyte pH, cation type, dissolved N_2 concentration, and boundary layer thickness.[32] Therefore, to further improve the NRR performance, a deep theoretical understanding of EDL formation and its effect on the NRR process are urgently required, which require the development of new theoretical methods. Recently, a continuum model for electrochemical N_2 reduction that includes both the NRR and the HER kinetics coupled to diffusive mass transport of solution species has been reported,[44] but without accounting for the steric hindrance of the ions and the effect of EDLs. Compared to the Poisson–Nernst–Planck (PNP) equations, the modified PNP (MPNP) equations include the effect of volume exclusion due to the solvated size of solution species, thus, providing a better description of EDLs in concentrated electrocatalytic systems.[45]

In this article, we develop a theoretical framework to study the reaction-transport process of the NRR system in an acidic aqueous electrolyte. The calculation is implemented by combining MPNP equations with a microkinetic model that features both the electrochemical NRR and HER kinetics.[44] The MPNP equations solve the migration, diffusion, and reaction processes self-consistently by accounting for steric effects which are ignored in PNP equations.[46] The comparison of MPNP and PNP calculations highlights the necessity of involving the steric effects in our study for the reaction-transport process. By implementing our approach, we describe the EDL structure near the cathode surface and then calculate the NRR performance under different applied electrode potential (E_p). The obtained data are based on input parameters typical for Au-based catalysts that are promising candidates for the electrosynthesis of NH_3 from N_2,[19,20] and compared to experimental results.[47] Moreover, the resistance of N_2 diffusion to the catalyst surface through the EDL is expected as an important factor in the activation mechanism of NRR. Therefore, we further study the influence of bulk electrolyte

concentration on the EDL structure and subsequently NRR performance. Finally, we analyze the interplay between N_2 diffusion and reaction activity under the nano-confinement.

2 | MODEL AND METHODS

2.1 | Model description

Figure 1A illustrates the NRR system in an acidic aqueous electrolyte. An individual nanopore of the porous cathode is considered to study the role of confinement (Figure 1B). As shown in Figure 1C, we focus on studying the influence of N_2 diffusion toward the cathode–electrolyte interface, including the roles of densely packed cations in the EDL, the kinetics of proton–electron transfer (ET; including the HER-competition) as well as the pore geometry. We consider an acidic aqueous electrolyte (pH = 1) under 1 atm N_2 partial pressure at room temperature (293.15 K), such that $c^0_{H^+} = 0.1$ M and $c^0_{N_2} = 7.14 \times 10^{-4}$ M (which corresponds to 19.98 mg N_2 per kg of water as measured by Morrison and Billet) in the bulk solution.[48] Upon applying a voltage E_p at the cathode with respect to the electrolyte reservoir, mass transport of H^+, Cl^-, and N_2 takes place in the pore driven by the combined NRR and HER at the cathode.

2.2 | MPNP equations

A classical description of EDL formation is given by the PNP equations for diffusive and conductive transport of dissolved species in a viscous dielectric continuum in contact with a charged solid wall.[49,50] The PNP equations implicitly assume all dissolved species to be point particles, an approximation that breaks down at high concentrations, for instance at concentrated bulk solutions or close to charged surfaces at overpotentials (far) beyond the thermal voltage of 25 mV where steric effects become quantitatively as well as qualitatively important.[46,51] Excluding steric effects can, for instance, lead to an unphysically high ionic concentration and an excessively high capacitance of the EDL.[46] For this reason in this article we use the MPNP equations to solve the dynamics of the mass transport of solution species including the effects of diffusion, packing, migration, as well as reaction, which incorporate a mean-field continuum description of steric effects to the PNP system. The modified Nernst–Planck equations used to the mass transport of solution species are given by[45,46,51]:

$$\frac{\partial c_i}{\partial t} = -\nabla \cdot \vec{J}_i, \tag{1}$$

$$\vec{J}_i = -D_i \nabla c_i - \frac{D_i z_i F c_i}{RT} \nabla \phi - D_i c_i \left(\frac{N_A \sum_{i=1}^{3} a^3 \nabla c_i}{1 - N_A \sum_{i=1}^{3} a^3 c_i} \right). \tag{2}$$

Here, c_i, D_i, and z_i are the concentration, the diffusion coefficient (see Table S1), and the charge valency ($z_1 = +1$, $z_2 = -1$, and $z_3 = 0$) of species i (1 for H^+, 2 for Cl^- and 3 for N_2), respectively. In addition, F, R, and T represent the Faraday constant, gas constant, and absolute temperature ($T = 293.15$ K), respectively, a is the effective diameter of the dissolved particles, and ϕ is the electrostatic potential that satisfies the Poisson equation:

$$\nabla \cdot (\varepsilon_0 \varepsilon_r \nabla \phi) = -F \sum_{i=1}^{n} z_i c_i, \tag{3}$$

where ε_0 is the permittivity of vacuum and ε_r is the relative permittivity of water ($\varepsilon_r = 78$). Here we set $a = 0.6$ nm and $a^{-3} = 7.7$ M throughout, which mimics the size of solvated H^+,[52] however for simplicity it is considered to be the effectively solvated diameter of all dissolved species.

Although this approach is less accurate than more advanced nonlocal approaches based on classical density functional theories for the hard-sphere fluid,[53–55] it does contain the essential physics of ionic packing while its computational efficiency allows for the required coupling to mass transport and chemical reactions in the nonplanar geometry of interest which will be discussed in the forthcoming sections. The MPNP equations actually only involve the introduction of a finite particle diameter a and a maximum local concentration a^{-3}, and it is well known from studies in planar geometries, for instance, that the MPNP equations give a more realistic account of the EDL properties at high potentials than their unmodified PNP counterparts.[51] The detailed derivation of MPNP equations for our system can be found in the Appendix S1.

As shown in Figure 2, our MPNP equations also involve the so-called outer-Helmholtz plane (OHP), which is the plane of closest approach for the dissolved ions of diameter a. The OHP, which we use as the cathode surface located at $z = 0$ in our coordinate system where $|d/2 - z|$ ($z \le d/2$) is the radial distance from the symmetry axis of the nanopore, is therefore not only the boundary of mass transport for solution species but also the reaction plane where we assume the NRR and the HER to take place. Moreover, the OHP also separates the EDL at the electrolyte side ($z > 0$) from the Stern layer of $\lambda_S = a/2$ ($-a/2 < z < 0$) toward the bulk electrode side. We also include the Stern capacitance by assuming the Stern layer to be uncharged with the imposed electrode potential E_p at $z \le -a/2$ rather than at $z = 0$, such that a potential drop takes place between the OHP and the electrode. Figure S2A shows the steady-state potential profile $\phi(z)$ in the nm-vicinity of the cathode for several electrode potentials E_p, where we note that E_p is not identical to the potential at the OHP ϕ_0 ($z = 0$) because of the Stern layer capacitance that we consider; in fact, we impose the boundary condition ϕ_e ($z = -0.3$ nm) $= E_p$.

2.3 | Reaction kinetics of HER and NRR

The significant ingredient of our MPNP equations involves the coupling of charge, potential, diffusion, and migration to the catalytic reactions at the surfaces of the porous cathode, for which we characterize both the NRR and the HER in terms of their corresponding rate-determining steps (RDSs). The HER is a typical two-ET reaction with one catalytic intermediate, as shown in Figure S3A. The possible

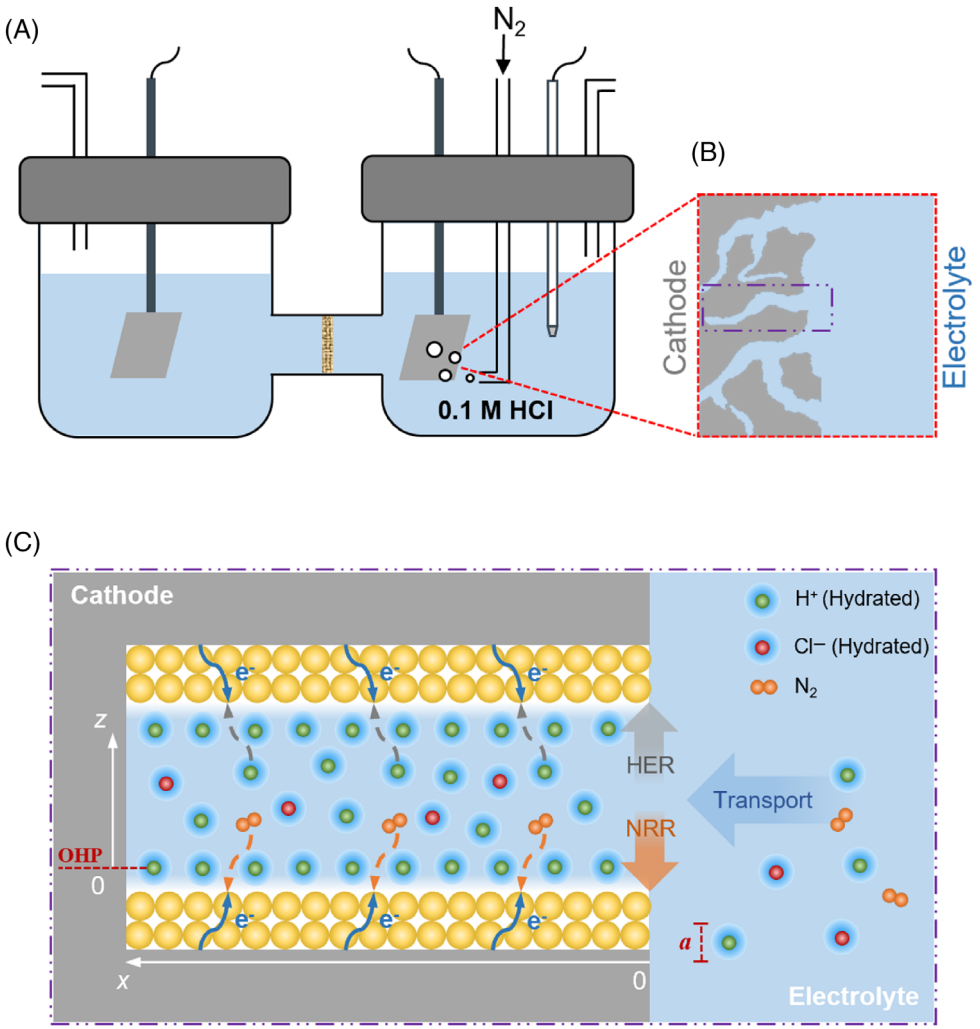

FIGURE 1 (A) Schematics of the setup for nitrogen reduction reaction (NRR) system. (B) Schematic diagram of the interface between a porous cathode and an aqueous HCl electrolyte with dissolved N_2. (C) Schematic illustration of the mass transport of N_2, hydrated H^+ and Cl^- in a single pore driven by the combined NRR and hydrogen evolution reaction at the cathode surface. The outer Helmholtz plane (OHP) is the closest approach for the dissolved ions, which is considered as the cathode surface ($z = 0$) here

pathway for HER can be considered as Volmer–Heyrovský mechanism or Volmer–Tafel mechanism, which depends on the catalyst material.[56] The rate of the overall reaction is largely determined by the hydrogen adsorption free energy. It is demonstrated that the Volmer step ($H^+ + e^- \rightarrow {}^*H$) determines the rate of the overall reaction at Au catalyst surfaces,[57] in which hydrogen binds to the surface too weakly, and the HER can be described by Butler–Volmer equation[58,59]:

$$i_{\mathrm{loc,HER}} = i_{0,\mathrm{HER}}\{\exp(-\alpha_c f\eta_H) - \exp[(1-\alpha_c)f\eta_H]\}, \quad (4)$$

with cathodic charge transfer coefficient $\alpha_c = 0.5$, $f = F/RT$ and exchange current density $i_{0,\mathrm{HER}}$. Experimental results for $i_{0,\mathrm{HER}}$ vary from 10^{-5} to 10^{0} mA/cm^2 for different metal surfaces; however, in this study we fix $i_{0,\mathrm{HER}} = 0.007$ mA/cm^2 as is typical for Au catalysts.[57] Of course the analysis can be extended to other catalysts. The electrochemical overpotential is $\eta_H = E_p$, calculated as the difference between applied electrode potential (E_p) and standard HER redox potential (0 V vs. reversible hydrogen electrode, RHE).[60]

The possible mechanisms for the NRR are illustrated in the Figure S3A. For the associative pathways, it has been demonstrated that the

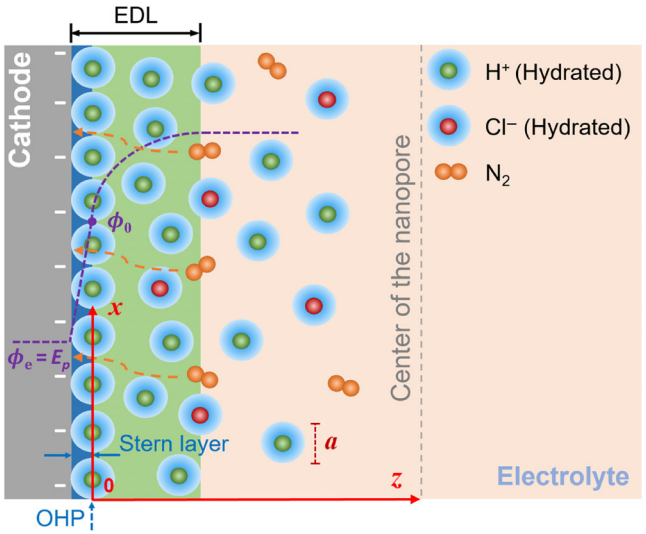

FIGURE 2 Schematic of the cathode–electrolyte interface involving the electric double layer region during nitrogen reduction reaction in an aqueous HCl electrolyte with dissolved N_2. The purple dotted curve in the electrolyte is a typical potential profile with ϕ_e and ϕ_0 being the potential of the metal cathode and at the outer Helmholtz plane (OHP)

RDS of the NRR at the Au catalyst surface is the first proton-coupled electron transfer (PCET) step, $N_{2(g)} + H^+ + e^- \rightarrow {}^*N_2H$, in which an adsorbed N_2 molecule not only captures an electron from the cathode but also a proton from solution.[15,17,40] We therefore divide the PCET into two elemental steps: the ET step, $N_{2(g)} + e^- \rightarrow *N_2^-$, and the proton transfer (PT) step, $*N_2^- + H^+ \rightarrow {}^*N_2H$.[44] The detailed derivations of the theoretical treatment of the two chemical reactions (ET and PT) are presented in Appendix S1, where we also introduce a phenomenological parameter for each of the two reactions to characterize the (quantum-) chemistry of the process, and thus yielding the local kinetic rate of the NRR process per unit surface area as:

$$i_{\mathrm{loc,NRR}} = \frac{i_{0,1,\mathrm{NRR}} \frac{c_{N_2}}{c^0_{N_2}} \exp(-\alpha_c f \eta_N)}{1 + \frac{i_{0,1,\mathrm{NRR}} c^0_{H^+}}{i_{0,2,\mathrm{NRR}} c_{H^+}} \exp(\alpha_c f \eta_N)}. \tag{5}$$

Accordingly, the two parameters can also be cast in the form of so-called exchange current densities, which we denote by $i_{0,1,\mathrm{NRR}}$ (for ET), and $i_{0,2,\mathrm{NRR}}$ (for PT). The nitrogen electrochemical overpotential is $\eta_N = E_p$ – 0.27 V, calculated as the difference between E_p and standard NRR redox potential (0.27 V vs. RHE). In order to select the two NRR parameters for Au-based catalyst, we study the influence of the $i_{0,1,\mathrm{NRR}}$ and $i_{0,2,\mathrm{NRR}}$ on the NRR performance by solving Equations (1)–(5) with a parametric sweep of the $i_{0,1,\mathrm{NRR}}$ varying from 10^{-6} to 10^{-2} mA/cm^2 and $i_{0,2,\mathrm{NRR}}$ varying from 10^{-10} to 10^{-2} mA/cm^2. Figure 3 displays the two-dimensional (2D) contour plot of (A–C) Faradaic efficiency (*FE*) and (D-F) NRR current density (i_{NRR}) as a function of $i_{0,1,\mathrm{NRR}}$ and $i_{0,2,\mathrm{NRR}}$ when $Ep = -0.1$ to -0.3 V vs. RHE, indicating that $i_{0,1,\mathrm{NRR}}$ is the key parameter determining the NRR reaction rate. Then, comparing to the experimental results of FE and i_{NRR} for Au catalysts,[47,61] which is nearly equal to the values at the left bottom of Figure 3, we thus set $i_{0,1,\mathrm{NRR}} = 7 \times 10^{-6}$ mA/cm^2 that is three orders of magnitudes lower than the corresponding HER case. Moreover, we cannot ignore the role of proton transfer (PT) process in the overall reaction,[44] and thus, a small value of $i_{0,2,\mathrm{NRR}}$ (10^{-10} mA/cm^2) with respect to the $i_{0,1,\mathrm{NRR}}$ is considered.

In addition to construct a database of {*FE*, i_{NRR}} with different combinations of {$i_{0,1,\mathrm{NRR}}$ and $i_{0,2,\mathrm{NRR}}$} for selecting the reasonable NRR parameters with regard to a specific system, the Tafel analysis can be also implemented to obtain corresponding NRR parameters. Empirically, the following Tafel relation has been well confirmed[62]:

$$\eta_N = a + b\log(i_{\mathrm{NRR}}), \tag{6}$$

where b is Tafel slope. According to the Tafel relation and the Butler–Volmer equation, the following equation can be derived:

$$\eta_N = \frac{\ln(i_{0,1,\mathrm{NRR}})}{\alpha_c f} - \frac{\ln(i_{\mathrm{NRR}})}{\alpha_c f}. \tag{7}$$

Then, fitting with the experimental data of η_N and i_{NRR}, the parameters $i_{0,1,\mathrm{NRR}}$ and α_c can be determined. Therefore, according to the NRR current density at -0.1 to -0.2 V in experiment,[47] the $i_{0,1,\mathrm{NRR}} = 1.12 \times 10^{-5}$ mA/cm^2 and $\alpha_c = 0.43$ is obtained. However, the simulation results calculated using the parameters do not fit well with the experimental profile, as shown in Figure S4, which has a lower current density and faradaic efficiency at high potentials. It indicates that the experimental data of the NRR performance cannot reflect the intrinsic activity of the electrocatalysts, and may include the effect of mass transport. Therefore, to obtain reliable kinetic parameters from this approach, the experimental data of η_N and i_{NRR} for the specific system need to be carefully selected by excluding the effect of solution environment and mass transport.

To characterize the performance of NRR, the mean current density of NRR for the whole nanochannel is calculated as:

$$i_{\mathrm{NRR}} = \frac{1}{A}\int i_{\mathrm{loc,NRR}} dA, \tag{8}$$

where A is surface area of the channel. The Faradaic efficiency *FE*, defined as the percentage of partial current density of NRR (i_{NRR}) within the total current density ($i_{\mathrm{total}} = i_{\mathrm{NRR}} + i_{\mathrm{HER}}$) that passes through the electrode surface, is expressed as:

$$\mathrm{FE} = \frac{i_{\mathrm{NRR}}}{i_{\mathrm{total}}} = \frac{i_{\mathrm{NRR}}}{i_{\mathrm{NRR}} + i_{\mathrm{HER}}} = \frac{\int i_{\mathrm{loc,NRR}} dA}{\int i_{\mathrm{loc,NRR}} dA + \int i_{\mathrm{loc,HER}} dA}. \tag{9}$$

2.4 | Simulation details

As shown in Figure S1, a 2D axisymmetric model was constructed for an electrochemical N_2 reduction system using COMSOL Multiphysics, a software package for finite element method (https:/www.comsol.com/). Equations (1)–(5) are solved simultaneously with the following initial and boundary conditions to obtain the species concentration and potential profiles at steady state. Dirichlet boundary conditions are used to fix the concentrations of species and potential in the bulk (AB boundary), including $c^0_{H^+} = c^0_{Cl^-} = 0.1$ M, $c^0_{N_2} = 7.14 \times 10^{-4}$ M, and potential $\phi = 0$. The initial conditions in the electrolyte for the concentrations and potential are assumed to be at bulk values. Zero-flux conditions are applied to the boundaries of BC, CD, and FG. A mixed boundary condition applies for the electrolyte potential ϕ_0 at the boundaries of DE and EF, which are considered as the OHP ($z = 0$):

$$\phi_0 + \lambda_S(\mathbf{n}\cdot\nabla\phi) = E_p, \tag{10}$$

where $\lambda_s = a/2 = 0.3$ nm is considered as the thickness of the Stern layer.[52] The condition can be reformulated as a surface charge condition that depends on the potential difference, $\phi_\Delta = E_p - \phi_0$, between the electrode potential E_p and the electrolyte potential ϕ_0 at the OHP:

$$\mathbf{n}\cdot(-\varepsilon_0\varepsilon_r\nabla\phi) = -\frac{\varepsilon_0\varepsilon_r\phi_\Delta}{\lambda_s}. \tag{11}$$

Meanwhile, based on the Equations (4) and (5) the flux conditions $\vec{J}_i$ are applied to the cathode surface (DE and EF boundaries) to describe

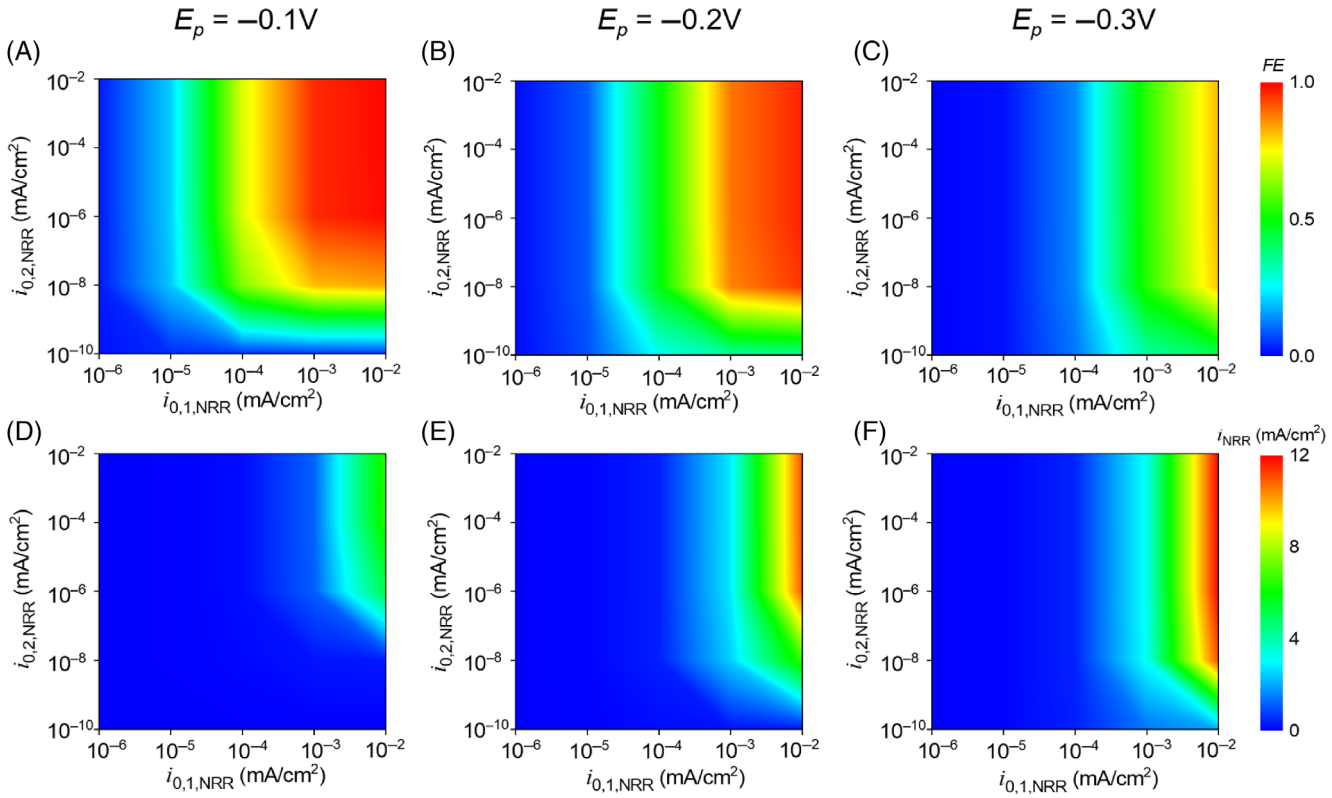

FIGURE 3 The role of different exchange current density ($i_{0,1,NRR}$, $i_{0,2,NRR}$) on the Nitrogen reduction reaction (NRR) reaction ($i_{0,HER} = 7 \times 10^{-3}$ mA/cm^2, $a = 0.6$ nm, $d = 50$ nm at bulk concentrations 0.1 M HCl and 7.14×10^{-4} M N_2). The two-dimensional contour plots of (A–C) Faradaic efficiency (FE) and (D–F) NRR current density (i_{NRR}) as a function of $i_{0,1,NRR}$ and $i_{0,2,NRR}$ with different electrode potentials

the heterogeneous reactions (NRR and HER) occurring at the OHP, and the overall NRR reaction in acidic solution is:

$$N_2(aq) + 6e^- + 8H^+ \rightarrow 2NH_4^+(aq), \tag{12}$$

and the overall HER reaction in acidic solution is:

$$2H^+(aq) + 2e^- \rightarrow H_2(aq). \tag{13}$$

The normal component of the flux of species i (H^+ and N_2) at the catalytic surfaces can be expressed as:

$$\mathbf{n} \cdot \vec{J}_i = R_{i,NRR} + R_{i,HER} = \frac{\nu_{i,NRR} i_{loc,NRR}}{n_{NRR} F} + \frac{\nu_{i,HER} i_{loc,HER}}{n_{HER} F}, \tag{14}$$

where $R_{i,NRR}$, $R_{i,HER}$, $\nu_{i,NRR}$, and $\nu_{i,HER}$ are the rate of production and the stoichiometric coefficient of species i for the NRR and HER, respectively, and $n_{NRR} = 6$, $n_{HER} = 2$, $i_{loc,NRR}$ and $i_{loc,HER}$ are the number of transfer electrons and the local current density for the overall reaction of the NRR and HER, respectively. Note that $\vec{J}_i = 0$ for species (Cl^-) that are not involved in the reactions, that is, the electrodes are blocking in that case. Here, to simplify the calculations, the products including NH_3, NH_4^+ and H_2 are not considered in our simulations, which we checked to have no significant influence on our main results.

3 | RESULTS AND DISCUSSION

3.1 | Comparison of MPNP and PNP equations

Based on the microkinetic data of Au-based catalyst, we investigate the potential and ionic concentration profiles in a relatively large pore (diameter $d = 50$ nm and length $L_{pore} = 500$ nm) when $E_p = -0.3$ V. Figure 4A–C presents the sectional distributions of potential, H^+ and N_2 concentrations inside this nanopore. We can see from Figure 4A that the potential at the cathode surface (ϕ_0) is screened by the EDL region which extends a few nanometers into the electrolyte. In that region, as shown in Figure 4B,C, a densely packed layer of cation ions is formed, and simultaneously a depletion of N_2 appears. Therefore, the condensed layer of cation ions in the EDL region is expected as the main origin of the resistance of N_2 diffusion to the catalyst surface. By contrast, the nanochannel is wide enough for the present case of slow surface reactions to replenish N_2 throughout the channel all the way to its dead end at $x = L_{pore} = 500$ nm. Therefore, as illustrated in these inset figures, the potential and ion concentrations within a few nanometers away from cathode surface are thus independent of the location along the axial x-direction.

To illustrate the dramatic effect on the N_2 diffusion by the steric hindrance of the cations in the EDL, we present in Figure 4D,E a comparison of MPNP and PNP calculations of the steady-state concentration profiles of H^+ and N_2 near the surface where the NRR and HER occur. One can

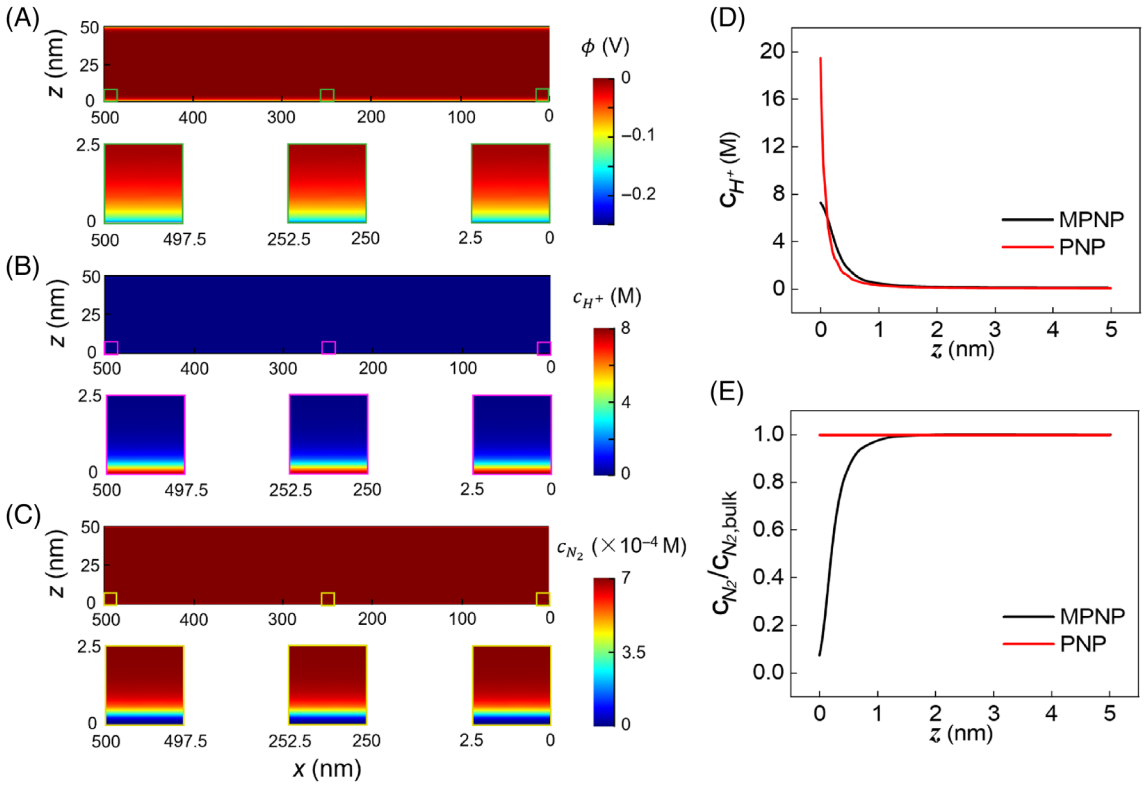

FIGURE 4 The sectional distributions of the potential (A), H^+ (B) and N_2 (C) concentrations inside the individual pore (diameter $d = 50$ nm and length $L_{pore} = 500$ nm) when applied electrode potential $E_p = -0.3$ V. The inset figures are the local distributions near the cathode surfaces. Comparison of the steady-state concentration profiles of H^+ (D, c_{H^+}) and N_2 (E, c_{N_2}) in the 5 nm-vicinity of the electric double layer region at the pore entrance ($x = 0$) as obtained from modified Poisson–Nernst–Planck (PNP) (finite particle size $a = 0.6$ nm) and PNP (point particles) for pore diameter $d = 50$ nm, voltage $E_p = -0.3$ V, electrolyte 0.1 M HCl, and saturated bulk nitrogen concentration 7.14×10^{-4} M

see from Figure 4D that the H^+ concentration at the cathode surface reaches unphysically high values in the PNP calculations, whereas the volume exclusion of the MPNP calculations restricts the maximum concentration to $a^{-3} = 7.7$ M. Furthermore, Figure 4E shows that the N_2 concentration from the MPNP theory tends to vanish almost completely in the nm-vicinity of the cathode surface, which is due to the close-packed monolayer of hydrated protons that are attracted to the cathode. By contrast, the N_2 concentration from the PNP calculations for point-particles does not lead to any exclusion of N_2 from the EDL region. Consequently, according to the plots (Figure S3C) of the logarithm of i_{NRR} as a function of the overpotential $\eta = E_p - E_0$, where E_p is the imposed electrode potential and E_0 is the equilibrium potential at which the electric current vanishes, the difference of the NRR current between PNP and MPNP is explicit at high absolute overpotentials $|\eta|$. These results highlight the importance of the steric effects in studying the influence of N_2 diffusion on the electrocatalytic N_2 reduction.

3.2 | Influence of EDL on NRR performance: theory vs. experiments

Then, the effect of the electrode potential on the EDL structure near cathode surface is further studied. Figure 5A–C illustrates the steady-state profiles of potential, H^+ and N_2 concentrations near the cathode surface and the pore mouth at different E_p. We can see from Figure 5A and Figure S2 that the E_p-dependent EDL structures screen the surface potential. In Figure 5B,C, one can find that for increasingly negative electrode potentials, more H^+ ions are electrostatically attracted to the cathode surface, which leads to a lower N_2 concentration near the cathode surface. The enhanced H^+ concentration and the reduced N_2 concentration at the cathode surface upon decreasing E_p toward −0.4 V are further quantified in Figure 5D. The pore-averaged concentrations $\langle c_{H^+} (z = 0) \rangle$ and $\langle c_{N_2} (z = 0) \rangle$ at the cathode surface reveals that $\langle c_{H^+} (z = 0) \rangle$ approaches the steric limit a^{-3} and $\langle c_{N_2} (z = 0) \rangle$ approaches zero for E_p as negative as −0.4 V. Indeed, due to the steric hindrance of the adsorbed H^+ ions, it is increasingly difficult for N_2 molecules to diffuse toward the cathode surface at deeply negative E_p.

On the basis of Equations (8) and (9), the current density of the NRR (i_{NRR}) and the Faradaic efficiency (*FE*) are calculated, and plotted together with experimental data for electrocatalytic NRR over the catalyst Au/TiO_2 in Figure 5E,F.[47] The i_{NRR} is a measure for the reaction rate of nitrogen reduction. Interestingly, Figure 5E reveals that our theoretical i_{NRR} (black curve) accurately reproduces the experimentally observed non-monotonic behavior with the electrode potential (red curve), although the peak in our calculations seems to be somewhat broader and shifted to $E_p = -0.3$ V compared to $E_p = -0.2$ V in the

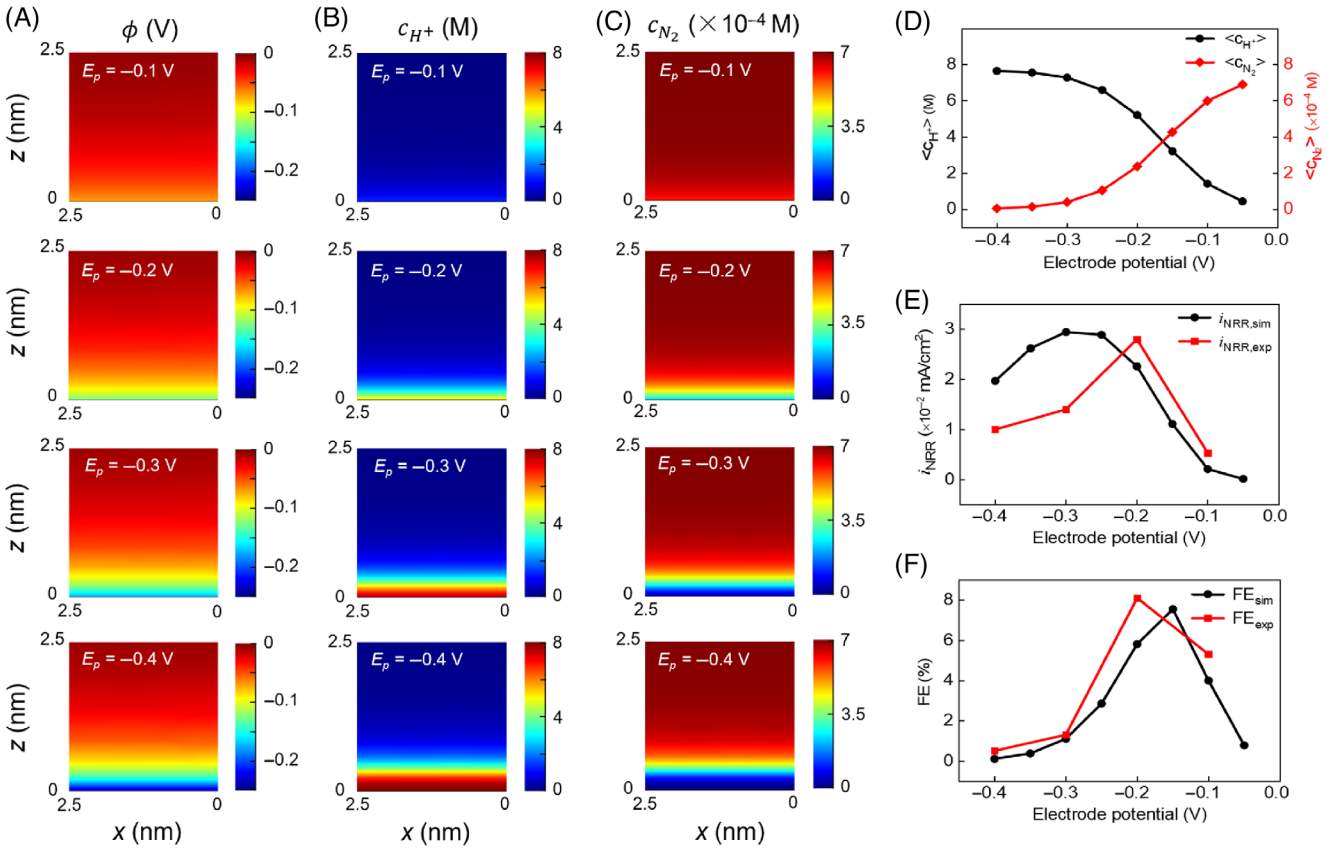

FIGURE 5 Nitrogen reduction reaction (NRR) performance for Au catalyst in nitrogen-saturated electrolyte (0.1 M HCl and 7.14×10^{-4} M N_2). The steady-state profiles of potential (A), H^+ (B), and N_2 (C) concentrations in a 2.5 nm × 2.5 nm region near the cathode surface ($z = 0$) and the pore mouth ($x = 0$) at different E_p. (D) The dependence on the electrode potential of the pore-averaged concentrations of H^+ ($<c_{H^+}>$) and N_2 ($<c_{N_2}>$) at the cathode surface. Comparison between simulation and experimental results of the NRR current density (E, i_{NRR}) and Faradaic efficiency (F, *FE*) as a function of the E_p

experiment. In fact, the phenomenon that the NRR rate decreases when the electrode potential becomes more negative than about −0.2 to −0.3 V was observed in several experiments,[47,61,63] which was speculated to be caused by the competitive adsorption of N_2 and hydrogen species on the electrode surface.[64,65] This speculation is now fully confirmed by our results as discussed above. Furthermore, both the predicted and the measured *FE* of the NRR system with the Au-based catalyst rise to about 8% at low potentials, as shown in Figure 5F, and then decrease significantly with high negative potentials. At high electrode potentials, the HER becomes the primary process, resulting in the *FE* reduction. Therefore, good catalysts for NRR should be highly active for nitrogen reduction at low electrode potential in order to improve the N_2 diffusion as well as suppress the HER.[66]

3.3 | Influence of H^+ concentration on NRR performance

We have seen that the build-up of the EDL has a negative influence on the diffusion of N_2 towards the catalyst surface, which limits the NRR performance, especially at deeply negative applied electrode potentials. We therefore expect that a reduction of the steric hindrance of accumulated cations in the EDL can improve the NRR performance. A key factor that determines the structure of the EDL is the bulk ion concentration c_{bulk}, which determines the Debye length $\lambda_D \propto 1/\sqrt{c_{bulk}}$ that sets the characteristic EDL thickness. In Figure 6A–C ($E_p = -0.2$ V), we present the potential, H^+ and N_2 concentration profiles in the nm-vicinity of the electrode surface for a fixed saturated N_2 concentration and a set of bulk HCl concentrations $c_{bulk} = 10^{-3}$, 10^{-2}, 10^{-1}, 10^{0} M. The potential distributions (Figure 6A) between the central axis (at $z = 25$ nm) and the cathode surface (at $z = 0$) illustrate that the EDL region is narrowed with concentrating the electrolyte solution, which is consistent with the description of the Debye length. However, as indicated in Figure 6B,C, a higher bulk H^+ concentration leads to an increased H^+ concentration and a reduced N_2 concentration close to the electrode surface. In addition, Figure 6D quantifies the pore-averaged concentrations $<c_{H^+}$ ($z = 0$)> and $<c_{N_2}$ ($z = 0$)> at the cathode surface, which illustrates that the adsorption of N_2 on the catalyst surface is largely limited at high bulk H^+ concentration. The variation of the bulk H^+ concentration would also affect the NRR performance as characterized by the i_{NRR} and FE (Figure 6E,F). At low bulk H^+ concentrations (10^{-4}, 10^{-5} M), the rate of the NRR is limited by limited transfer of protons for the protonation of nitrogen species.

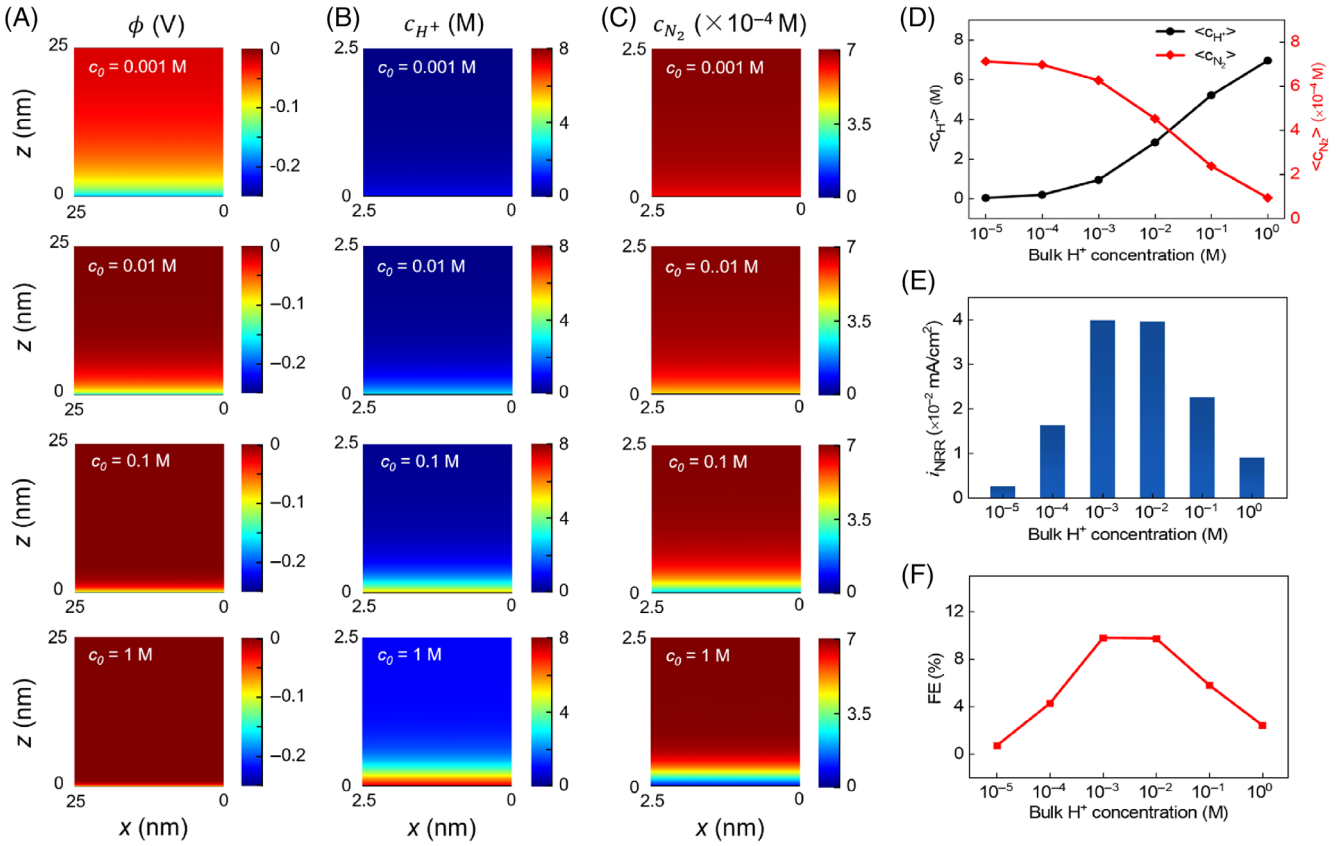

FIGURE 6 Nitrogen reduction reaction (NRR) performance for Au catalyst with different bulk H^+ concentrations ($E_p = -0.2$ V and 7.14×10^{-4} M N_2). (A) The potential distributions (25 nm × 25 nm) as well as the concentration distributions (2.5 nm × 2.5 nm) of H^+ (B) and N_2 (C) in the region near the cathode surface. (D) The pore-averaged concentrations of H^+ (<c_{H^+}>) and N_2 (<c_{N_2}>) at the cathode surface as a function of the bulk H^+ concentration. (E) The NRR current density (i_{NRR}) and (F) Faradaic efficiency (*FE*) at each given bulk H^+ concentration

At high bulk H^+ concentration (10^{-1}, 10^0 M), the NRR is also suppressed by the strong competition of the HER. Consequently, an enhanced NRR performance can be obtained with a 100-fold dilution of the 0.1 M HCl used above down to 10^{-3} M (pH = 3). Interestingly, these theoretical findings can be verified by an experimental investigation that selects an optimized pH value of 3.5 by testing the NRR performance in N_2-saturated electrolytes with different pH values.[23] Furthermore, Figure S5 illustrates that this H^+ dilution effect depends on the electrode potentials. For instance, at low electrode potential ($E_p = -0.1$ V), the concentration of H^+ ions accumulated near the cathode surface is low, and hence the EDL has little influence on the N_2 diffusion. By contrast, the proton transfer process is limited by the reduced proton concentration, which results in the decrease of the NRR rate and Faradaic efficiency upon proton dilution.

3.4 | Promoting NRR performance by enhancing N_2 diffusion

As discussed above, at deeply negative electrode potentials the NRR rate is limited by the reduced diffusion of N_2 through the EDL to the cathode surface, which can be partially mitigated by diluting the electrolyte. Also, several additional strategies can be implemented to improve the NRR rate of an electrocatalyst system, for instance by engineering the channel dimensions of the nanostructured electrode (here modeled by d and L_{pore}) or the intrinsic activity of active sites (here represented by the exchange current density $i_{0,1,NRR}$ that characterize the ET step for the NRR).[67] We consider here the dependence of the NRR efficiency on the pore size by comparing the cases $d = 50$ nm and $d = 10$ nm, as well as on the $i_{0,1,NRR}$, which is the parameter that essentially determines the catalyst activity as we show in Figure 3. Firstly, Figure 7A,B display the concentration distributions of N_2 in the two channels of diameter 10 and 50 nm at four different NRR reactivity parameters $i_{0,1,NRR}$ from 10^{-6} to 10^{-3} mA/cm^2, where an experimental realization of the high-end of $i_{0,1,NRR}$ requires the development of new catalysts to accelerate the NRR. Due to the low solubility of N_2 in the aqueous electrolyte, increasing the NRR rate leads to a significant depletion of N_2 deep in the channel, the more so for narrower channels. This reveals that the steric hindrance of the solution species on the diffusion of N_2 from bulk reservoir to the smaller channel interior is a key feature of these systems. Furthermore, we present a comparison between the N_2 concentrations on the cathode surface of the two different channels along x-direction for $i_{0,1,NRR} = 10^{-5}$ and 10^{-3} mA/cm^2 in Figure 7C. When the NRR rate is fast, the surface N_2 concentration is significantly reduced beyond $x = 10$–100 nm away from the inlet at $x = 0$, however less so for the larger pore diameters. The increase of the pore size is therefore favorable

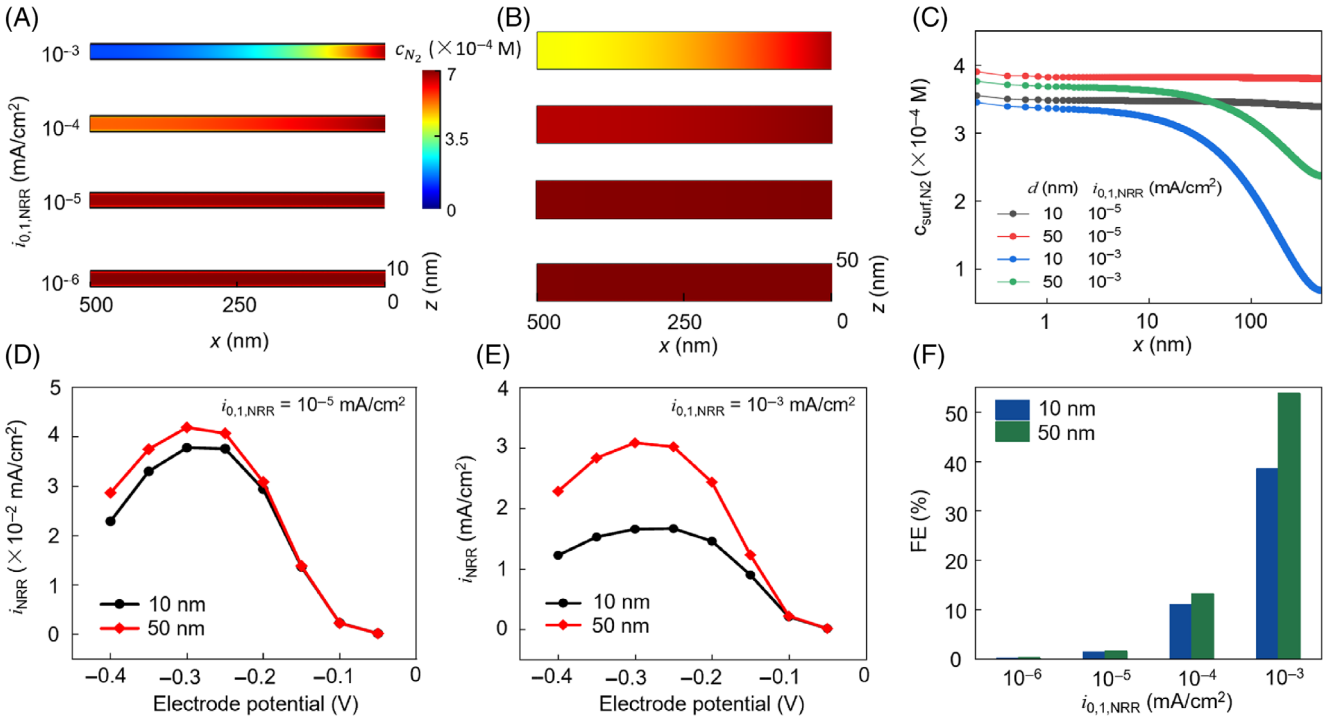

FIGURE 7 Nitrogen reduction reaction (NRR) performance for different catalyst activities in a small or large pore ($E_p = -0.3$ V, 0.1 HCl and 7.14×10^{-4} M N_2). The concentration distributions of N_2 in the two different nanochannels (A, $d = 10$ nm, and B, $d = 50$ nm) with the $i_{0,1,NRR}$ increasing from 10^{-6} to 10^{-3} mA/cm^2. (C) Surface concentration of N_2 (c_{surf,N_2}) along the x direction with pore sizes of 10 and 50 nm for $i_{0,1,NRR} = 10^{-5}$ and 10^{-3} mA/cm^2. The NRR current density (i_{NRR}) vs. electrode potential for pore diameter $d = 10$ and 50 nm when $i_{0,1,NRR} = 10^{-5}$ mA/cm^2 (D) and $i_{0,1,NRR} = 10^{-3}$ mA/cm^2 (E). (F) Faradaic efficiency (*FE*) of the whole nanochannel with pore diameter of 10 and 50 nm for $i_{0,1,NRR} = 10^{-6}$–10^{-3} mA/cm^2

for the adsorption of N_2 on the cathode surface and hence improves the i_{NRR} and FE, the more so for the faster NRR reaction rate as can be seen in Figure 7D,E. As shown in Figure 7F, an increase of $i_{0,1,NRR}$ up to 10^{-4} or 10^{-3} mA/cm^2 can increase the FE up to 11% or even 38%, the more so for larger pore diameters. The calculation results for more pore sizes are summarized in Figure S6, which indicates that comparing to the H^+ transport, the N_2 diffusion in the highly active electrocatalytic system is more sensitive to the pore size.

Consequently, analyzing the effect of electrode microstructure needs to consider the activity of the catalyst: if the intrinsic activity of each active site or the loading of the catalyst materials is low, which is the case for most of presently available catalysts, a pore size of 10 or 50 nm has little influence on the NRR performance. However, if the activity of the electrocatalyst is improved, the limited N_2 diffusion in smaller pores cannot be ignored and causes, as we show, a depletion of N_2 deep in the channel. In this case it is therefore beneficial to increase the pore size (for the present choice of parameters) beyond 10 nm to enhance the N_2 diffusion. Interestingly, recent research has shown that some single-atom catalysts (Fe, Ru, and Mo) exhibit superior NRR performance,[22,27,68] and hence these catalysts are more likely to suffer from diffusion limitations when loaded onto porous electrodes. Therefore, for practical design of nanostructured electrodes, a balance needs to be found between small pores with large catalytic surfaces and larger pores with optimal transport properties.

4 | CONCLUSIONS

In this article, we have investigated the coupled reaction-transport processes in an electrocatalytic NRR system and evaluated the NRR performance under different experimental conditions using an effective continuum model. We find that the potential- and concentration-dependent EDL as well as the reaction-induced N_2 concentration gradients play vital roles on the NRR activity and selectivity. At deeply negative electrode potentials, the aggregated cations in the EDL near the cathode surface will hinder N_2 diffusion from the electrolyte in the channel to the cathode surface, thereby reducing adsorption on active sites, thus limiting the reaction rate of NRR. As practical electrodes for NRR have ambiguous and irregular microstructures, which can increase the number of active sites on the electrode, nanochannels with different sizes are considered here to study how the nano-confinement influences the reaction environment and the performance of the catalyst. The effect of pore size on the NRR performance becomes significant if the NRR rate is high, which leads to a depletion of N_2 in the smallest internal nanochannels. Based on our discussion above on the effect of the EDL and the interplay between N_2 diffusion and surface reduction reaction, we hope our research can provide theoretical guidance to the understanding and design of advanced electrocatalytic systems for nitrogen reduction.

ACKNOWLEDGMENTS

This work is part of the D-ITP consortium, a program of the Netherlands Organization for Scientific Research (NWO) that is funded by the Dutch Ministry of Education, Culture and Science (OCW). We acknowledge the EU-FET project NANOPHLOW (REP-766972-1). This work was also sponsored by the National Natural Science Foundation of China (No. 91834301, 22078088), the National Natural Science Foundation of China for Innovative Research Groups (No. 51621002), and the Shanghai Rising-Star Program (No. 21QA1401900).

CONFLICT OF INTEREST

The authors declare no conflict of interest.

AUTHOR CONTRIBUTIONS

Haolan Tao: Conceptualization (equal); data curation (equal); formal analysis (equal); investigation (equal); methodology (equal); software (equal); validation (equal); visualization (lead); writing – original draft (lead); writing – review and editing (equal). **Cheng Lian:** Conceptualization (lead); data curation (equal); formal analysis (equal); funding acquisition (lead); investigation (equal); methodology (equal); project administration (lead); resources (equal); software (equal); supervision (lead); validation (lead); visualization (equal); writing – original draft (lead); writing – review and editing (equal). **Hao Jiang:** Data curation (equal); formal analysis (equal); investigation (equal); resources (equal); supervision (equal); writing – original draft (equal); writing – review and editing (equal). **Chunzhong Li:** Formal analysis (equal); project administration (equal); resources (equal); supervision (equal). **Honglai Liu:** Formal analysis (equal); funding acquisition (equal); project administration (equal); resources (lead); software (equal); supervision (lead); validation (equal). **René van Roij:** Conceptualization (equal); data curation (equal); formal analysis (equal); funding acquisition (equal); investigation (equal); methodology (lead); project administration (equal); resources (equal); software (equal); supervision (lead); validation (lead); visualization (equal); writing – original draft (lead); writing – review and editing (equal).

DATA AVAILABILITY STATEMENT

The data that supports the findings of this study are available in the supplementary material of this article.

ORCID

Haolan Tao https://orcid.org/0000-0003-4436-9144
Cheng Lian https://orcid.org/0000-0002-9016-832X
Hao Jiang https://orcid.org/0000-0002-4388-6548
Chunzhong Li https://orcid.org/0000-0001-7897-5850
Honglai Liu https://orcid.org/0000-0002-5682-2295
René van Roij https://orcid.org/0000-0002-2221-294X

REFERENCES

1. Seh ZW, Kibsgaard J, Dickens CF, Chorkendorff I, Nørskov JK, Jaramillo TF. Combining theory and experiment in electrocatalysis: insights into materials design. *Science*. 2017;355(6321):eaad4998.
2. Smil V. Detonator of the population explosion. *Nature*. 1999; 400(6743):415-415.
3. Rosca V, Duca M, de Groot MT, Koper MTM. Nitrogen cycle electrocatalysis. *Chem Rev*. 2009;109(6):2209-2244.
4. Schlögl R. Catalytic synthesis of ammonia—a "never-ending story"? *Angew Chem Int Ed*. 2003;42(18):2004-2008.
5. Vegge T, Sørensen RZ, Klerke A, et al. Indirect hydrogen storage in metal ammines. *Solid-State Hydrogen Storage*. Elsevier; 2008:533-564.
6. Schlögl R. Ammonia synthesis. *Handbook of Heterogeneous Catalysis*. 2nd ed. Wiley-VCH Verlag GmbH & Co. KGaA; 2008:2501-2575.
7. Philibert C. *Renewable Energy for Industry*. International Energy Agency; 2017.
8. Shipman MA, Symes MD. Recent progress towards the electrosynthesis of ammonia from sustainable resources. *Catal Today*. 2017; 286:57-68.
9. Kyriakou V, Garagounis I, Vasileiou E, Vourros A, Stoukides M. Progress in the electrochemical synthesis of ammonia. *Catal Today*. 2017; 286:2-13.
10. Guo C, Ran J, Vasileff A, Qiao S-Z. Rational design of electrocatalysts and photo (electro) catalysts for nitrogen reduction to ammonia (NH_3) under ambient conditions. *Energ Environ Sci*. 2018;11(1):45-56.
11. Tang C, Qiao S-Z. How to explore ambient electrocatalytic nitrogen reduction reliably and insightfully. *Chem Soc Rev*. 2019;48(12):3166-3180.
12. Van der Ham CJM, Koper MTM, Hetterscheid DGH. Challenges in reduction of dinitrogen by proton and electron transfer. *Chem Soc Rev*. 2014;43(15):5183-5191.
13. Lee HK, Koh CSL, Lee YH, et al. Favoring the unfavored: selective electrochemical nitrogen fixation using a reticular chemistry approach. *Sci Adv*. 2018;4(3):eaar3208.
14. Singh AR, Rohr BA, Schwalbe JA, et al. Electrochemical ammonia synthesis-the selectivity challenge. *ACS Catal*. 2017;7:706-709.
15. Deng J, Iñiguez JA, Liu C. Electrocatalytic nitrogen reduction at low temperature. *Joule*. 2018;2(5):846-856.
16. Chen JG, Crooks RM, Seefeldt LC, et al. Beyond fossil fuel-driven nitrogen transformations. *Science*. 2018;360(6391):eaar6611.
17. Montoya JH, Tsai C, Vojvodic A, Nørskov JK. The challenge of electrochemical ammonia synthesis: a new perspective on the role of nitrogen scaling relations. *ChemSusChem*. 2015;8(13):2180-2186.
18. Foster SL, Bakovic SIP, Duda RD, et al. Catalysts for nitrogen reduction to ammonia. *Nat Catal*. 2018;1(7):490-500.
19. Yao C, Guo N, Xi S, et al. Atomically-precise dopant-controlled single cluster catalysis for electrochemical nitrogen reduction. *Nat Commun*. 2020;11(1):4389.
20. Xue ZH, Zhang SN, Lin YX, et al. Electrochemical reduction of N2 into NH3 by donor-acceptor couples of Ni and au nanoparticles with a 67.8% faradaic efficiency. *J Am Chem Soc*. 2019;141(38):14976-14980.
21. Zheng J, Liao F, Wu S, et al. Efficient non-dissociative activation of dinitrogen to ammonia over lithium-promoted ruthenium nanoparticles at low pressure. *Angew Chem Int Ed*. 2019;58(48):17335-17341.
22. Tao H, Choi C, Ding L-X, et al. Nitrogen fixation by Ru single-atom electrocatalytic reduction. *Chem*. 2019;5(1):204-214.
23. Hao Y-C, Guo Y, Chen L-W, et al. Promoting nitrogen electroreduction to ammonia with bismuth nanocrystals and potassium cations in water. *Nat Catal*. 2019;2(5):448-456.
24. Cao N, Chen Z, Zang K, et al. Doping strain induced bi-Ti(3+) pairs for efficient N2 activation and electrocatalytic fixation. *Nat Commun*. 2019;10(1):2877.
25. Li J, Chen S, Quan F, et al. Accelerated dinitrogen electroreduction to ammonia via interfacial polarization triggered by single-atom protrusions. *Chem*. 2020;6(4):885-901.
26. Zhang S, Jin M, Shi T, et al. Electrocatalytically active Fe-(O-C2)4 single-atom sites for efficient reduction of nitrogen to ammonia. *Angew Chem Int Ed*. 2020;59(32):13423-13429.
27. Wang M, Liu S, Qian T, et al. Over 56.55% Faradaic efficiency of ambient ammonia synthesis enabled by positively shifting the reaction potential. *Nat Commun*. 2019;10(1):341.

28. Zang W, Yang T, Zou H, et al. Copper single atoms anchored in porous nitrogen-doped carbon as efficient pH-universal catalysts for the nitrogen reduction reaction. *ACS Catal*. 2019;9(11):10166-10173.
29. Han L, Ren Z, Ou P, et al. Modulating single-atom palladium sites with copper for enhanced ambient ammonia electrosynthesis. *Angew Chem Int Ed*. 2021;60(1):345-350.
30. Lin YX, Zhang SN, Xue ZH, et al. Boosting selective nitrogen reduction to ammonia on electron-deficient copper nanoparticles. *Nat Commun*. 2019;10(1):4380.
31. Ren Y, Yu C, Tan X, Huang H, Wei Q, Qiu J. Strategies to suppress hydrogen evolution for highly selective electrocatalytic nitrogen reduction: challenges and perspectives. *Energ Environ Sci*. 2021;14(3):1176-1193.
32. Kani NC, Prajapati A, Collins BA, Goodpaster JD, Singh MR. Competing effects of pH, cation identity, H2O saturation, and N2 concentration on the activity and selectivity of electrochemical reduction of N2 to NH3 on electrodeposited cu at ambient conditions. *ACS Catal*. 2020;10(24):14592-14603.
33. Liu S, Qian T, Wang M, et al. Proton-filtering covalent organic frameworks with superior nitrogen penetration flux promote ambient ammonia synthesis. *Nat Catal*. 2021;4(4):322-331.
34. Lazouski N, Chung M, Williams K, Gala ML, Manthiram K. Non-aqueous gas diffusion electrodes for rapid ammonia synthesis from nitrogen and water-splitting-derived hydrogen. *Nat Catal*. 2020;3(5):463-469.
35. Andersen SZ, Statt MJ, Bukas VJ, et al. Increasing stability, efficiency, and fundamental understanding of lithium-mediated electrochemical nitrogen reduction. *Energ Environ Sci*. 2020;13(11):4291-4300.
36. Battino R, Rettich TR, Tominaga T. The solubility of nitrogen and air in liquids. *J Phys Chem Ref Data Monogr*. 1984;13(2):563-600.
37. Choi J, Suryanto BHR, Wang D, et al. Identification and elimination of false positives in electrochemical nitrogen reduction studies. *Nat Commun*. 2020;11(1):5546.
38. Andersen SZ, Čolić V, Yang S, et al. A rigorous electrochemical ammonia synthesis protocol with quantitative isotope measurements. *Nature*. 2019;570(7762):504-508.
39. Suryanto BHR, Du H-L, Wang D, Chen J, Simonov AN, MacFarlane DR. Challenges and prospects in the catalysis of electroreduction of nitrogen to ammonia. *Nat Catal*. 2019;2(4):290-296.
40. Skulason E, Bligaard T, Gudmundsdottir S, et al. A theoretical evaluation of possible transition metal electro-catalysts for N_2 reduction. *Phys Chem Chem Phys*. 2012;14(3):1235-1245.
41. Liu X, Jiao Y, Zheng Y, Jaroniec M, Qiao S-Z. Building up a picture of the electrocatalytic nitrogen reduction activity of transition metal single-atom catalysts. *J Am Chem Soc*. 2019;141(24):9664-9672.
42. Choi C, Gu GH, Noh J, Park HS, Jung Y. Understanding potential-dependent competition between electrocatalytic dinitrogen and proton reduction reactions. *Nat Commun*. 2021;12(1):4353.
43. Dunwell M, Yan Y, Xu B. Understanding the influence of the electrochemical double-layer on heterogeneous electrochemical reactions. *Curr Opin Chem Eng*. 2018;20:151-158.
44. Lu S, Lee DH, Liu C. Modeling of electrocatalytic dinitrogen reduction on microstructured electrodes. *Small Methods*. 2019;3(6):1800332.
45. Bohra D, Chaudhry JH, Burdyny T, Pidko EA, Smith WA. Modeling the electrical double layer to understand the reaction environment in a CO_2 electrocatalytic system. *Energ Environ Sci*. 2019;12(11):3380-3389.
46. Kilic MS, Bazant MZ, Ajdari A. Steric effects in the dynamics of electrolytes at large applied voltages. I double-layer charging. *Phys Rev E*. 2007;75(2):021502.
47. Shi MM, Bao D, Wulan BR, et al. Au sub-nanoclusters on TiO_2 toward highly efficient and selective electrocatalyst for N_2 conversion to NH_3 at ambient conditions. *Adv Mater*. 2017;29(17):1606550.
48. Kolev NI. Solubility of O2, N2, H2 and CO2 in water. *Multiphase Flow Dynamics 4: Turbulence, Gas Adsorption and Release, Diesel Fuel Properties*. Springer-Verlag; 2012:209-239.
49. Newman J, Thomas-Alyea EK. *Electrochemical Systems*. John Wiley & Sons; 2004.
50. Lyklema J. *Solid-Liquid Interface*. SERBIULA (sistema Librum 2.0). Fundamentals of interface and colloid science. Vol II; Academic Press; 1995.
51. Kilic MS, Bazant MZ, Ajdari A. Steric effects in the dynamics of electrolytes at large applied voltages. II modified Poisson-Nernst-Planck equations. *Phys Rev E*. 2007;75(2):021503.
52. Nightingale ER. Phenomenological theory of ion solvation. Effective radii of hydrated ions. *J Phys Chem*. 1959;63(9):1381-1387.
53. Lian C, Zhao S, Liu H, Wu J. Time-dependent density functional theory for the charging kinetics of electric double layer containing room-temperature ionic liquids. *J Chem Phys*. 2016;145(20):204707.
54. Lian C, Su H, Li C, Liu H, Wu J. Non-negligible roles of pore size distribution on electroosmotic flow in nanoporous materials. *ACS Nano*. 2019;13(7):8185-8192.
55. Liu Y. Multiscale mechanisms of reaction-diffusion process in electrode systems: a classical density functional study. *Chem Eng Sci*. 2020;227:115899.
56. Kibler LA. Hydrogen electrocatalysis. *ChemPhysChem*. 2006;7(5):985-991.
57. Nørskov JK, Bligaard T, Logadottir A, et al. Trends in the exchange current for hydrogen evolution. *J Electrochem Soc*. 2005;152(3):J23.
58. Zheng Y, Jiao Y, Jaroniec M, Qiao S. Advancing the electrochemistry of the hydrogen-evolution reaction through combining experiment and theory. *Angew Chem Int Ed*. 2015;54(1):52-65.
59. Zeng M, Li Y. Recent advances in heterogeneous electrocatalysts for the hydrogen evolution reaction. *J Mater Chem*. 2015;3(29):14942-14962.
60. Bard AJ, Parsons R, Jordan J. *Standard Potentials in Aqueous Solution*. Marcel Dekker; 1985:138.
61. Bao D, Zhang Q, Meng F-L, et al. Electrochemical reduction of N_2 under ambient conditions for artificial N_2 fixation and renewable energy storage using N_2/NH_3 cycle. *Adv Mater*. 2017;29(3):1604799.
62. Shinagawa T, Garcia-Esparza AT, Takanabe K. Insight on Tafel slopes from a microkinetic analysis of aqueous electrocatalysis for energy conversion. *Sci Rep*. 2015;5:13801.
63. Yang X, Nash J, Anibal J, et al. Mechanistic insights into electrochemical nitrogen reduction reaction on vanadium nitride nanoparticles. *J Am Chem Soc*. 2018;140(41):13387-13391.
64. Oshikiri T, Ueno K, Misawa H. Selective dinitrogen conversion to ammonia using water and visible light through plasmon-induced charge separation. *Angew Chem Int Ed*. 2016;55(12):3942-3946.
65. Cheng H, Cui P, Wang F, Ding LX, Wang H. High efficiency electrochemical nitrogen fixation achieved with a lower pressure reaction system by changing the chemical equilibrium. *Angew Chem Int Ed*. 2019;58(43):15541-15547.
66. Zhao H, Zhang D, Wang Z, et al. High-performance nitrogen electroreduction at low overpotential by introducing Pb to Pd nanosponges. *Appl Catal Environ*. 2020;265:118481.
67. Benck JD, Hellstern TR, Kibsgaard J, Chakthranont P, Jaramillo TF. Catalyzing the hydrogen evolution reaction (HER) with molybdenum sulfide nanomaterials. *ACS Catal*. 2014;4(11):3957-3971.
68. Zhao J, Chen Z. Single Mo atom supported on defective boron nitride monolayer as an efficient electrocatalyst for nitrogen fixation: a computational study. *J Am Chem Soc*. 2017;139(36):12480-12487.

SUPPORTING INFORMATION

Additional supporting information may be found in the online version of the article at the publisher's website.

How to cite this article: Tao H, Lian C, Jiang H, Li C, Liu H, van Roij R. Enhancing electrocatalytic N_2 reduction via tailoring the electric double layers. *AIChE J*. 2022;68(3):e17549. doi:10.1002/aic.17549